Evaluation of a Novel Elastic Respiratory Motion Correction Algorithm on Quantification and Image Quality in Abdominothoracic PET/CT

Joseph G. Meier[1], Carol C. Wu[2], Sonia L. Betancourt Cuellar[2], Mylene T. Truong[2], Jeremy J. Erasmus[2], Samuel A. Einstein[1], and Osama R. Mawlawi[1]

[1]Department of Imaging Physics, University of Texas M.D. Anderson Cancer Center, Houston, Texas; and [2]Department of Diagnostic Radiology, University of Texas M.D. Anderson Cancer Center, Houston, Texas

Our aim was to evaluate in phantom and patient studies a recently developed elastic motion deblurring (EMDB) technique that makes use of all the acquired PET data and compare its performance with other conventional techniques such as phase-based gating (PBG) and HD·Chest (HDC), both of which use fractions of the acquired data. Comparisons were made with respect to static whole-body (SWB) images with no motion correction. **Methods:** A phantom simulating respiratory motion of the thorax with lung lesions (5 spheres with internal diameters of 10–28 mm) was scanned with 0, 1, 2, and 3 cm of motion. Four reconstructions were performed: SWB, PBG, HDC, and EMDB. For PBG, the average (PBG_{ave}) and maximum bin (PBG_{max}) were used. To compare the reconstructions, the ratios of SUV_{max}, SUV_{peak}, and contrast-to-noise ratio (CNR) were calculated with respect to SWB. Additionally, 46 patients with lung or liver tumors less than 3 cm in diameter were studied. Measurements of SUV_{max}, SUV_{peak}, and CNR were made for 46 lung and 19 liver lesions. To evaluate image noise, the SUV SD was measured in healthy lung and liver tissue and in the phantom background. Finally, the subjective image quality of patient examinations was scored on a 5-point scale by 4 radiologists. **Results:** In the phantom, EMDB increased SUV_{max} and SUV_{peak} over SWB but to a lesser extent than the other reconstruction methodologies. The ratio of CNR with respect to SWB for EMDB, however, was higher than all other reconstructions (0.68 with EMDB > 0.54 with HDC > 0.41 with PBG_{max} > 0.31 with PBG_{ave}). Similar results were seen in patient studies. SUV_{max} and SUV_{peak} were higher by, respectively, 19.3% and 11.1% with EMDB, 21.6% and 13.9% with HDC, 22.8% and 12.8% with PBG_{ave}, and 45.6% and 26.8% with PBG_{max}, compared with SWB. Lung and liver noise increased with EMDB by, respectively, 3% and 15%, with HDC by 35% and 56%, with PBG_{ave} by 100% and 170%, and with PBG_{max} by 146% and 219%. CNR increased in lung and liver tumors only with EMDB (18% and 13%, respectively) and decreased with HDC (−14% and −23%), PBG_{ave} (−39% and −63%), and PBG_{max} (−18% and −46%). The average radiologist scores of image quality were 4.0 ± 0.8 with SWB, 3.7 ± 1.0 with EMDB, 3.1 ± 1.0 with HDC, and 1.5 ± 0.7 with PBG. **Conclusion:** The EMDB algorithm had the least increase in image noise, improved lesion CNR, and had the highest overall image quality score.

Static whole-body (SWB) PET acquisitions typically last 2–3 min per bed position, which can result in degraded PET image quality due to respiratory motion, particularly for tumors in the lower thorax and upper abdomen (*1–3*). This degradation potentially results in decreased measurements of activity concentration, overestimated measured metabolic volume, and decreased lesion detectability, all of which could negatively affect patient management.

Many solutions exist to correct respiratory motion artifacts in PET/CT (*4–10*). However, all such methods first require the acquisition of the patient's respiratory waveform using external devices or data-driven techniques. One of the first motion correction methods proposed was multibin respiratory gating, which divides the acquired PET data into multiple bins corresponding to different respiratory phases or amplitudes of the breathing cycle. Fractioning the data into multiple bins increases the amount of noise per bin, however, which biases quantitative measures such as SUV_{max} and decreases image quality. These drawbacks can be overcome by a longer acquisition time but come at the expense of decreased patient comfort and reduced scanner throughput. Furthermore, whereas this approach allows the full range of tumor motion to be determined, which is crucial for radiation therapy planning, it increases the complexity of the interpretation because it results in multiple image volumes corresponding to the different bins.

Another approach to reduce motion while avoiding the complexity of multibin respiratory gating is end-expiration respiratory gating (*8,11*). End-expiration respiratory gating is based on the observation that patients tend to spend more time in the end-expiration quiescent period of the breathing cycle, which corresponds to the least amount of motion (*12*). In comparison to an individual bin of multibin respiratory gating, end-expiration respiratory gating has the advantage of using a larger fraction of the acquired PET data, resulting in less image noise while reducing motion blur, and creates only one PET volume for interpretation. End-expiration respiratory gating can be implemented using the amplitude or phase of the respiratory

waveforms. In the phase-based approach, PET data corresponding to a preset phase offset and window width from the onset of each breathing cycle are retained. This approach is implemented commercially on GE Healthcare PET/CT scanners as Q.Static (13). In the amplitude-based approach of end-expiration respiratory gating, implemented commercially as HD·Chest (HDC) on Siemens PET/CT scanners, the user selects a percentage of the acquired PET data to preserve (8,14–16). The HDC algorithm analyzes the respiratory waveform to find the minimum amplitude range that contains the user-selected percentage of PET data, typically about 35%. End-expiration respiratory gating, whether phase- or amplitude-based, has emerged as the most common respiratory motion correction because of its simplicity and ease of use.

Elastic motion correction is another approach for respiratory motion correction that retains all the acquired PET data to create the final image. Using the entirety of PET data improves image quality, thereby reducing the acquisition times that are typical in respiratory motion–corrected examinations. Two primary approaches exist for elastic motion correction. In one strategy, multibin respiratory gating images are reconstructed, nonrigidly registered, and then averaged into a single volume (17).This approach has been implemented commercially by GE Healthcare as Q.Freeze. A more recent approach (implemented commercially by Siemens and known as OncoFreeze) first derives a blurring kernel from subimages (SWB and HDC) that are later used during image reconstruction to generate the final motion-free image (18,19). To our knowledge, there has been no independent evaluation of the elastic motion deblurring (EMDB) algorithm with the exception of one small-scale study (5 patients) presented as an abstract (20).

In this study, we evaluated these various respiratory motion correction methodologies (multibin respiratory gating, amplitude-based optimal gating, and EMDB) in comparison to SWB with no motion correction. Initially, a phantom evaluation was performed to provide a comparison of these algorithms with respect to the ground truth. We then assessed the impact of these various approaches on clinical PET lesion quantification as well as objective and subjective image quality. Numerous publications have studied the impact of multibin respiratory gating and HDC, but to the best of our knowledge, this is the first investigation that systematically compared the EMDB algorithm with other motion-correction techniques.

MATERIALS AND METHODS

Reconstruction Algorithms

In this study, 4 PET reconstructions were investigated. The first was SWB, which used all the data, with no respiratory motion correction. The second was multibin respiratory gating, which reconstructed 8 gates (each containing 12.5% of the PET data). The third was HDC, which used the manufacturer-recommended 35% duty cycle for reconstruction. The fourth was the EMDB algorithm (18,19), which used 100% of the acquired PET data to reconstruct a motion-corrected image.

The EMDB algorithm initially performs an SWB reconstruction with 100% of the data and an HDC reconstruction that applies a baseline shift-correction to the patient respiratory waveform. In this study, we used a 35% duty cycle for the HDC image. The EMDB algorithm uses mass preservation optical flow (21) to non-rigidly register the reference volume (HDC) to the target volume (SWB) as seen in Figure 1. The HDC volume and the SWB volume have the same integral activity, but because of motion blur, the objects in each respective volume have different

brightness, necessitating the mass preservation optical flow algorithm to register the 2 volumes. Mass preservation optical flow does not require that the motion vectors correspond to physically realizable motion. EMDB uses mass preservation optical flow to determine a fully 3-dimensional blurring kernel to redistribute the activity between the HDC SWB volumes. In the EMDB reconstruction, the blurring kernel is applied to the current image estimate before forward projection. The transpose of the blurring kernel, the deblurring kernel, is applied after backprojection and results in a motion-corrected image estimate as seen in Figure 1.

Phantom Evaluation

A phantom was constructed to move 5 spheres in 3 dimensions to simulate the elastic motions of the abdomen and thorax. A detailed phantom description is provided as supplemental material (supplemental materials are available at http://jnm.snmjournals. org). The spheres had inner diameters of 10, 13, 17, 22, and 28 mm. The spheres were placed in an acrylic tank containing 16 L of water, and the sphere-to-background ratio was set to 5:1. A motor drove the spheres using a repeated patient respiratory cycle that had a duration of 6 s. Four acquisitions were performed in which the spheres were driven with amplitudes of 0, 1, 2, and 3 cm. The phantom motion was programmed such that the spheres always returned to the same location for all acquisitions. The phantom was scanned on a 4-ring Siemens Biograph mCT Flow system, which has previously been characterized (22). CT-based attenuation correction data were acquired while the spheres were motionless and at the initial position. The PET data were acquired during continuous bed motion for 60 cm. In each acquisition, 3 table-speed zones were prescribed: 1 mm/s for the 15 cm superior to the acrylic tank, 0.5 mm/s for the 30 cm covering the phantom tank, and 1 mm/s for the 15 cm inferior to the phantom tank. During PET acquisition, the respiratory waveform was acquired with the AZ-733V respiratory gating system (Anzai Medical Co.) (23) by wrapping the belt around the surrogate motor platform (Fig. 2). The phantom and setup are shown in Figures 2A and
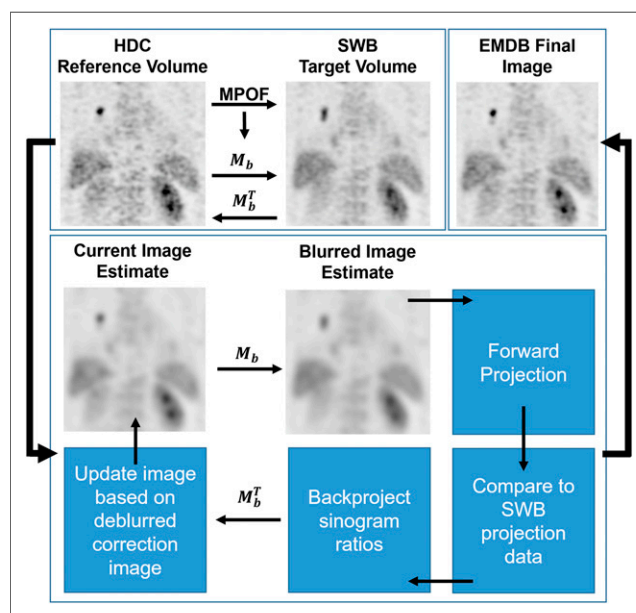
FIGURE 1. Workflow of EMDB algorithm. MPOF = mass preservation optical flow.
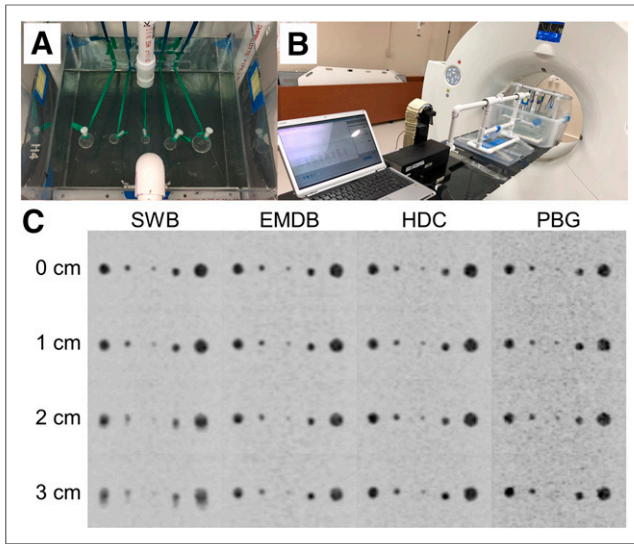
FIGURE 2. Phantom experimental setup and results. (A) Acrylic tank and spheres. (B) Spheres driven in superior–inferior direction by dynamic thorax phantom motor (right). (C) Maximum-intensity-projection images of phantom for 4 phantom acquisitions with varying motion and 4 reconstruction methods: SWB, EMDB, HDC, and PBG (1/8 gates).

2B and the supplemental material. Each phantom scan was 15 min. Care was taken to ensure that each acquisition had similar counting statistics, using list-mode rebinning of the acquired data. SWB, EMDB, HDC, and phase-based gating (PBG) reconstructions were performed for all phantom scans. All reconstructions were performed with the default clinical parameters: 2 iterations, 21 subsets, time-of-flight information, point-spread-function correction, a 200×200 matrix, $4.07 \times 4.07 \times 3$ mm voxels, and isotropic gaussian postfiltration of 5 mm in full width at half maximum.

For each motion amplitude and reconstruction algorithm, we measured SUV_{max}, SUV_{peak}, and SUV SD. SUV_{max} and SUV_{peak} were determined from a region of interest encompassing each sphere. All measurements were made in MIM, version 6.6 (MIM Software, Inc.). SUV SD was measured in the uniform background of the phantom with a 3-cm-diameter spheric region of interest. Contrast-to-noise ratio (CNR) for each sphere was also calculated according to Equation 1 using the sphere SUV_{max} (SUV_{max},sp), background SUV_{max} (SUV_{max},bg), and background SUV SD (σ).

$$\text{CNR} = \frac{SUV_{max}, sp - SUV_{max}, bg}{\sigma}. \qquad \text{Eq. 1}$$

For each sphere, phantom scan, and reconstruction, the SUV ratio and the CNR ratio relative to the SUV and CNR of the ground-truth SWB reconstruction with no motion was calculated for SUV_{max}, SUV_{peak}, and CNR. For the measurements made on the 8 gates of the PBG reconstruction, the average value of all 8 gates was used (PBG_{ave}), as well as the gate with the highest value (PBG_{max}) for each respective measurement of SUV_{max}, SUV_{peak}, SUV SD, and CNR. The average SUV SD was calculated for all background spheres, phantom scans, and reconstruction algorithms.

Patient Evaluation

Forty-six patients (23 men and 23 women; mean age, 62.9 ± 14.8 y; mean body mass index, 28.2 ± 6.7) with 65 lung ($n = 46$) or liver ($n = 19$) lesions in regions affected by respiratory motion and less than 3 cm in diameter were prospectively recruited for this study. The institutional review board approved this study

(approval 2015-0989), and all subjects gave written informed consent before undergoing imaging. Patients fasted for 6 h before injection of 323 ± 56 MBq of ^{18}F-FDG. The PET scan followed the ^{18}F-FDG injection by 69.2 ± 9.1 min.

### PET/CT Acquisition and Image Reconstruction

All patients were scanned with the same PET/CT system and protocols as used for the phantom scans, except that the patient PET data were acquired in continuous bed motion with a table speed of 0.8–1 mm/s, depending on patient body mass index. Over the lung/liver region where tumor was affected by motion, a table speed of 0.5 mm/s was used for a 30-cm section of the scan. Patient respiratory waveforms were acquired with the Anzai system. All CT scans were acquired with free breathing. SWB, EMDB, HDC, and PGB reconstructions were performed for all patient scans, with the same reconstruction parameters as used for the phantom scans.

Image Analysis

SUV_{max} and SUV_{peak} normalized by body weight were measured for each tumor. SUV SD (a surrogate for image noise) was measured using a 3-cm-diameter spheric region of interest in lung and liver tissue that we assessed to be free of disease. The CNR was calculated analogously to Equation 1. All measurements were made in MIM, version 6.6. For the PBG reconstruction, both PBG_{ave} and PBG_{max} were analyzed.

Image Quality Assessment

Four radiologists who were experienced in PET/CT imaging subjectively scored the image quality of the 4 reconstructions on a Likert-type scale of 1 (poor) to 5 (excellent). In total, 184 reconstructions (46 patients × 4 reconstructions) were assessed. For the PBG reconstructions, gate 5/8 was selected for presentation because it contained the least motion. Only one reconstruction at a time was displayed for assessment. The order of the presentation was randomized by reconstruction method and patient. Only the images acquired from the 30-cm region scanned with a 0.5 mm/s table speed were presented for image quality scoring. To assess intrareader reliability, 20 cases were repeated.
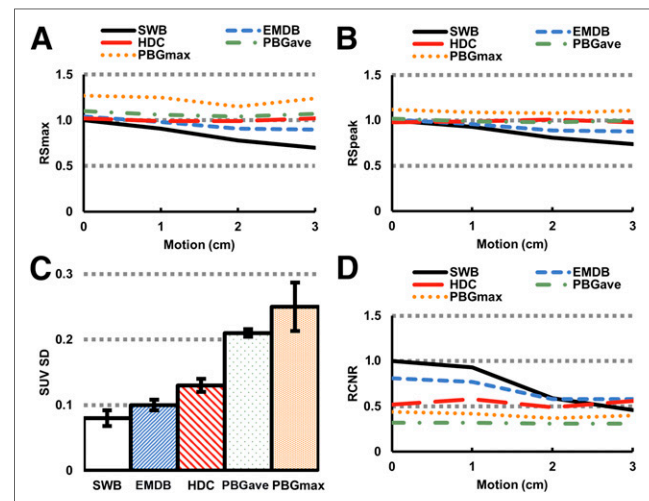
FIGURE 3. Phantom experimental measurements. (A and B) SUV_{max} normalized to SWB (RSmax) (A) and SUV_{peak} normalized to SWB (RSpeak) (B) variation due to sphere displacement. (C) SUV SD in background across all reconstructions. (D) CNR ratio normalized to SWB (RCNR) variation due to sphere displacement. Data are for average of all spheres.

Statistical Analysis

All statistical analyses were performed with R (version 3.5.0 and package "irr," version 0.84). Wilcoxon signed-rank tests, with Bonferroni adjustments, were performed to determine significance. The α-test of Krippendorf (24) was used to assess inter- and intrareader reliability in image quality assessment.

RESULTS

Phantom Evaluation

All motion correction methodologies successfully reduced image blur (Fig. 2C). The average values of SUV_{max} normalized to SWB over all spheres and motion amplitudes were 0.85 with SWB, 0.96 with EMDB, 1.01 with HDC, 1.06 with PBG_{ave}, and 1.23 with PBG_{max} (Fig. 3A). The average values of SUV_{peak} normalized to SWB were 0.87 with SWB, 0.94 with EMDB, 0.99 with HDC, 1.00 with PBG_{ave}, and 1.10 with PBG_{max} (Fig. 3B). Only the SWB and EMDB reconstructions had decreasing SUV_{max} normalized to SWB and SUV_{peak} normalized to SWB with increasing sphere motion amplitude. The sphere with the smallest inner diameter (10 mm) had the largest decreases in SUV_{max} normalized to SWB and in SUV_{peak} normalized to SWB as the motion amplitude increased. The percentage increases in SUV SD compared with the SWB reconstruction were 24.6% with EMDB, 61.6% with HDC, 171.7% with PBG_{ave}, and 216.2% with PBG_{max} (Fig. 3C). The average values of CNR ratio normalized to SWB were 0.31 with PBG_{ave}, 0.41 with PBG_{max}, 0.54 with HDC, 0.68 with EMDB, and 0.74 with SWB (Fig. 3D). Motion correction did not increase CNR ratio normalized to SWB above the SWB value until the motion amplitude reached 3 cm, and this was only for the EMDB and HDC reconstructions (Fig. 3D). Decreases in CNR ratio normalized to SWB relative to motion amplitude were observed only for the SWB and EMDB reconstructions (Fig. 3D).

Patient Tumor Quantification

In comparison to the SWB reconstruction, all motion-correcting reconstruction algorithms displayed significant increases in SUV_{max} and SUV_{peak} (Fig. 4A). The percentage increases in SUV_{max} in comparison to SWB for EMDB, HDC, PBG_{ave}, and PBG_{max} were 19.3%, 21.6%, 22.8%, and 45.6%, respectively. The percentage increases in SUV_{peak} in comparison to SWB for EMDB, HDC, PBG_{ave}, and PBG_{max} were 11.1%, 13.9%, 12.8%, and 26.8%, respectively. For measurements of both SUV_{max} and SUV_{peak}, PBG_{max} had the largest increase in comparison to SWB, whereas PBG_{ave}, HDC, and EMDB had relatively similar increases, with EMDB consistently having the lowest values. The percentage increases in lung and liver SUV SD in comparison to SWB for EMDB, HDC, PBG_{ave}, and PBG_{max} were, respectively, 3.3% and 14.8%, 35.1% and 55.8%, 100.0% and 169.6%, and 145.8% and 219.0% (Fig. 4B), showing that EMDB consistently had the least increase in lung and liver SUV SD. Across all motion correction methodologies, the increases in SUV SD were higher in the liver than in the lung. The percentage increases for lung and liver lesion CNR in comparison to SWB for EMDB, HDC, PBG_{ave}, and PBG_{max} were, respectively, 17.8% and 13.3%, −13.9% and −23.2%, −38.6% and −62.7%, and −18.2% and −46.0%. EMBD was the only motion correction method that increased lesion CNR (the others had negative results), although the increase in liver lesion CNR was not significant ($P = 0.58$). Example patient images of all 4 reconstructions are shown in Figure 5.
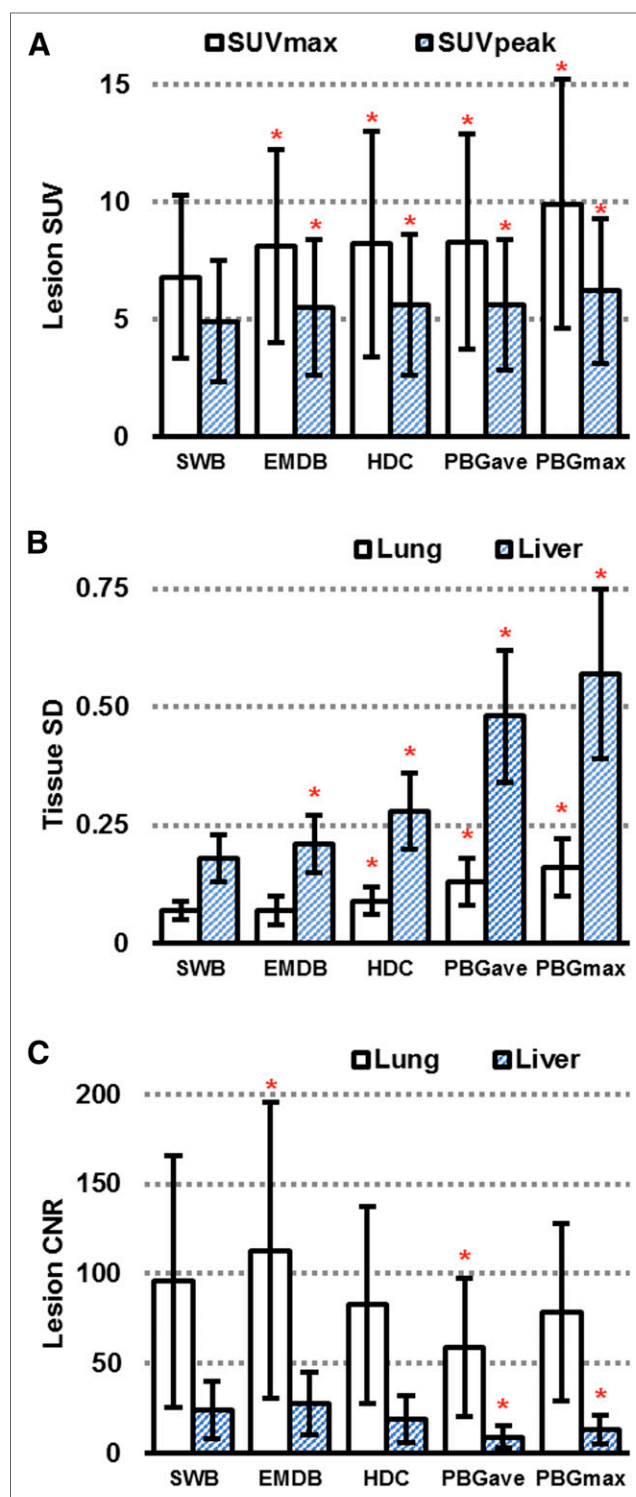

FIGURE 4. SUV_{max} and SUV_{peak} for 65 lesions (A), SUV SD for lung and liver tissue (B), and CNR for lung and liver lesions (C). *$P < 0.01$.

Subjective Image Quality

Of the motion correction methods, EMDB was scored as having the best overall image quality (Fig. 6). The percentage changes in image quality in comparison to SWB for EMDB, HDC, and PBG were −9.7%, −22.6%, and −63.7%, respectively. The intrareader
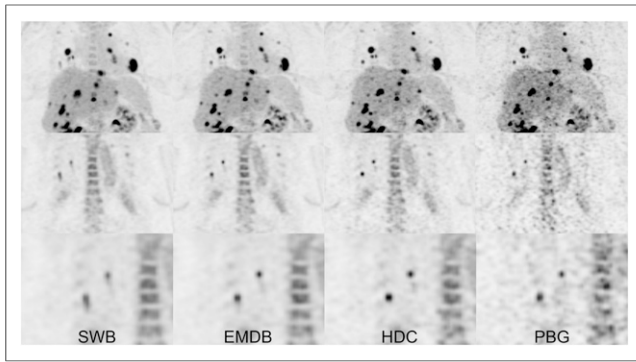
FIGURE 5. Example patient images. (Top) Maximum-intensity-projection images of all reconstructions. (Middle) Coronal plane view of right lung tumors. (Bottom) Zoomed view of middle row.

repeatability α-scores were 0.75, 0.77, 0.78, and 0.87, respectively. The interreader repeatability α-score was 0.81.

DISCUSSION

We assessed the impact of various motion correction methodologies on PET/CT imaging, with a primary interest in evaluating the EMDB technique. To our knowledge, this is the first published study on the impact of the EMDB algorithm in comparison with other motion correction methodologies in a relatively large cohort of patients.

The most important finding was that the EMDB algorithm had the smallest increase in image noise while reducing motion blur and improving lesion contrast. The primary cause of the reduced image noise was that the algorithm used all the acquired PET data, as opposed to use of a smaller fraction of the data by the other motion correction methodologies. These findings were consistent for both phantom and patient studies and were corroborated by the objective physician evaluation.

Although the EMDB algorithm used all the acquired PET data in the reconstruction, the resultant images still had increased noise when compared with SWB. We postulate that this noise resulted from the determination of the blurring kernel between the noisy HDC image and the SWB image in the EMDB algorithm. Specifically, the blurring kernel is influenced by the noise in the HDC image. In this regard, the choice of the percentage duty cycle for the HDC image has an important consequence on EMDB image quality. Increasing the duty cycle would reduce noise but at the expense of increased image blur, whereas decreasing the duty cycle has the opposite effect.
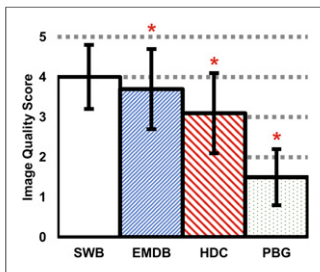
FIGURE 6. Mean image quality score for different reconstructions. Error bars represent 1 SD. *$P < 0.01$.

Several investigators have previously shown that image blur is reduced when using PET data corresponding to only a small fraction of the breathing cycle (25,26). However, one significant consideration when implementing such motion correction approaches is the artifactual increase in measured SUV_{max} and SUV_{peak} due to increased image noise. As seen in our phantom and patient results,

SUV_{max} and SUV_{peak} increased for all motion correction methodologies. However, these increases were amplified with decreasing amounts of PET data. Our phantom results indicate that image noise increased with methods that use decreasing amounts of PET data (increasing from 24.6% for EMDB to 216.2% for the PBG_{max} approach). In this regard, an increase in SUV_{max} or SUV_{peak} when using such correction techniques should be attributed not only to motion correction but also to an increase in image noise. In this work, we used CNR as a metric to capture both these image attributes (SUV_{max} and noise), and the results clearly show a decrease in CNR with correction methodologies that use decreasing amounts of PET data (Fig. 3D), reflecting the larger increase in image noise compared with a true increase in SUV_{max}.

One important finding about the EMDB algorithm is its degraded performance with increasing motion amplitude. Our results indicate that although all other motion correction methodologies resulted in an SUV_{max} and SUV_{peak} that were relatively independent of motion amplitude, the EMDB algorithm decreased these values with increasing motion but to a lower extent than SWB (Figs. 3A and 3B). It is not clear why this performance was observed, and further investigation is warranted.

In patient data, the percentage increases in SUV_{max} and SUV_{peak} were similar for EMDB, HDC, and PBG_{ave}. However, PBG_{max} had the highest percentage increases. The large differences seen between SUV for PBG_{max} and for the other motion correction methodologies is attributed to increases in image noise. EMDB had the least noise increase, yet the increases in SUV_{max} and SUV_{peak} were similar to HDC and PBG_{ave}, which use much less of the data. We can infer that the increases in SUV for the EMDB algorithm were influenced more by reductions in motion blur and less by increases due to noise bias.

EMDB was the only method that improved CNR, although not significantly for liver lesions, primarily because of the relatively high noise in the liver that neutralized any increase in liver SUV. Overall, however, EMDB increased SUV_{max} and SUV_{peak} yet had the least increase in image noise and, as a result, was the only method to improve lesion CNR. Although SUV_{max} and SUV_{peak} increased for the other motion correction methodologies, all of them decreased the CNR of the lesions.

Our image quality scores confirmed our expectations of low scores with increased image noise. Of the motion correction methodologies, the EMDB algorithm had the highest overall score, presumably because it contained the least image noise. The SWB images incurred substantial respiratory motion blur in comparison to the motion correction methodologies; however, the image quality scores showed that the primary concern in overall image quality was the amount of image noise present. In addition, we found good agreement between readers. A meta-analysis of the physician scores showed that in 50% of the cases, the physicians scored the EMBD images as having quality similar to or better than the SWB images. This number was 25% for cases in which the physicians scored the EMDB as strictly better than the SWB images. These results suggest that physicians either preferred images with reduced blur or could not perceive changes in background noise between these 2 reconstruction algorithms.

One limitation of this study was that patient CT-based attenuation correction data were acquired under free-breathing conditions. The literature has shown that mismatches in free-breathing CT and PET data often occur in areas affected by respiratory motion and can affect SUV quantification (27,28). It is possible that the quantification results of this study were affected

by these attenuation correction mismatches. Recent work in collaboration with our group has investigated the effects of these mismatches and have developed approaches to mitigate them (29). However, it would be interesting to assess the effect of such mismatches specifically on the performance of the EMDB algorithm as compared with other techniques.

Another limitation of this study was that all motion correction methods with the exception of the EMDB were performed without baseline shift correction of the respiratory waveform. (The EMDB algorithm had this feature embedded in the software.) In some patients, however, there can be a baseline drift in the respiratory waveform throughout the course of the examination that could affect the results of the various correction methods. In this regard, this data processing difference might have biased the results in favor of the EMDB algorithm. Analysis of the results with baseline shift for all the other correction methods will be a focus of future investigations.

CONCLUSION

All methods of motion correction reduced image blur but increased image noise, resulting in increased SUVs. The EMDB algorithm had the least noise increase, which resulted in improved CNR and higher image quality scores.

DISCLOSURE

ACKNOWLEDGMENTS

REFERENCES

1. Nehmeh SA, Erdi YE, Ling CC, et al. Effect of respiratory gating on reducing lung motion artifacts in PET imaging of lung cancer. *Med Phys.* 2002;29:366–371.
2. Frood R, McDermott G, Scarsbrook A. Respiratory-gated PET/CT for pulmonary lesion characterization: promises and problems. *Br J Radiol.* 2018;91:20170640.
3. Crivellaro C, De Ponti E, Elisei F, et al. Added diagnostic value of respiratory-gated 4D ¹⁸F-FDG PET/CT in the detection of liver lesions: a multicenter study. *Eur J Nucl Med Mol Imaging.* 2018;45:102–109.
4. Nehmeh SA, Erdi YE, Meirelles GSP, et al. Deep-inspiration breath-hold PET/CT of the thorax. *J Nucl Med.* 2007;48:22–26.
5. Dawood M, Büther F, Lang N, Schober O, Schäfers KP. Respiratory gating in positron emission tomography: a quantitative comparison of different gating schemes. *Med Phys.* 2007;34:3067–3076.
6. Qiao F, Clark JW, Pan T, Mawlawi O. Joint model of motion and anatomy for PET image reconstruction. *Med Phys.* 2007;34:4626–4639.
7. Chang G, Chang T, Pan T, Clark JW, Mawlawi OR. Joint correction of respiratory motion artifact and partial volume effect in lung/thoracic PET/CT imaging. *Med Phys.* 2010;37:6221–6232.
8. van Elmpt W, Hamill J, Jones J, De Ruysscher D, Lambin P, Öllers M. Optimal gating compared to 3D and 4D PET reconstruction for characterization of lung tumours. *Eur J Nucl Med Mol Imaging.* 2011;38:843–855.
9. Nehmeh SA. Respiratory motion correction strategies in thoracic PET-CT imaging. *PET Clin.* 2013;8:29–36.
10. Kesner AL, Meier JG, Burckhardt DD, Schwartz J, Lynch DA. Data-driven optimal binning for respiratory motion management in PET. *Med Phys.* 2018;45:277–286.
11. Frey K, Hamill J, Jones J, Koeppe R. Respiratory motion gated PET with end-expiratory, amplitude based gating [abstract]. *J Nucl Med.* 2009;50(suppl 2):348.
12. Liu C, Pierce LA II, Alessio AM, Kinahan PE. The impact of respiratory motion on tumor quantification and delineation in static PET/CT imaging. *Phys Med Biol.* 2009;54:7345–7362.
13. Hope TA, Verdin EF, Bergsland EK, Ohliger MA, Corvera CU, Nakakura EK. Correcting for respiratory motion in liver PET/MRI: preliminary evaluation of the utility of bellows and navigated hepatobiliary phase imaging. *EJNMMI Phys.* 2015;2:21.
14. Van Der Gucht A, Serrano B, Hugonnet F, Paulmier B, Garnier N, Faraggi M. Impact of a new respiratory amplitude-based gating technique in evaluation of upper abdominal PET lesions. *Eur J Radiol.* 2014;83:509–515.
15. Grootjans W, de Geus-Oei L-F, Troost EGC, Visser EP, Oyen WJG, Bussink J. PET in the management of locally advanced and metastatic NSCLC. *Nat Rev Clin Oncol.* 2015;12:395–407.
16. Hamill J, Ghosh P. White paper: HD·Chest amplitude-based respiratory gating for PET. Siemens website. https://static.healthcare.siemens.com/siemens_hwem-hwem_ssxa_websites-context-root/wcm/idc/groups/public/@global/@imaging/@molecular/documents/download/mdax/ntk5/~edisp/whitepaper01_hd.chest.2-00838487.pdf. Published 2011. Accessed October 11, 2018.
17. Dawood M, Buther F, Xiaoyi Jiang, Schafers KP. Respiratory motion correction in 3-D PET data with advanced optical flow algorithms. *IEEE Trans Med Imaging.* 2008;27:1164–1175.
18. Hong I, Jones J, Casey M. Ultrafast elastic motion correction via motion deblurring. In: *2014 IEEE Nuclear Science Symposium and Medical Imaging Conference (NSS/MIC).* Piscataway, NJ: IEEE; 2014:M10-97.
19. Hong I, Jones J, Hamill J, Michel C, Casey M. Elastic motion correction for continuous bed motion whole-body PET/CT. In: *2016 IEEE Nuclear Science Symposium, Medical Imaging Conference and Room-Temperature Semiconductor Detector Workshop (NSS/MIC/RTSD).* Piscataway, NJ: IEEE; 2016:M16B-6.
20. Poesse S, Hong I, Mannweiler D, et al. Respiratory motion compensation in PET/CT: evaluation of a fast elastic motion compensation technique based on motion deblurring [abstract]. *J Nucl Med.* 2017;58(suppl 1):1349.
21. Dawood M, Gigengack F, Jiang X, Schäfers KP. A mass conservation-based optical flow method for cardiac motion correction in 3D-PET. *Med Phys.* 2013;40:012505.
22. Rausch I, Cal-González J, Dapra D, et al. Performance evaluation of the Biograph mCT Flow PET/CT system according to the NEMA NU2-2012 standard. *EJNMMI Phys.* 2015;2:26.
23. Li XA, Stepaniak C, Gore E. Technical and dosimetric aspects of respiratory gating using a pressure-sensor motion monitoring system. *Med Phys.* 2006;33:145–154.
24. Krippendorff K. Reliability in content analysis. *Hum Commun Res.* 2006;30:411–433.
25. Bettinardi V, Rapisarda E, Gilardi MC. Number of partitions (gates) needed to obtain motion-free images in a respiratory gated 4D-PET/CT study as a function of the lesion size and motion displacement. *Med Phys.* 2009;36:5547–5558.
26. Liu C, Alessio A, Pierce L, et al. Quiescent period respiratory gating for PET/CT. *Med Phys.* 2010;37:5037–5043.
27. Pan T, Mawlawi O, Nehmeh SA, et al. Attenuation correction of PET images with respiration-averaged CT images in PET/CT. *J Nucl Med.* 2005;46:1481–1487.
28. Erdi YE, Nehmeh SA, Pan T, et al. The CT motion quantitation of lung lesions and its impact on PET-measured SUVs. *J Nucl Med.* 2004;45:1287–1292.
29. Hamill J, Mawlawi O, Meier J. Respiratory phase matching in PET/CT using fast spiral CT [abstract]. *J Nucl Med.* 2017;58(suppl 1):577.